

# The sensitivity of convection from a horizontal boundary to the distribution of heating

M. A. COMAN, R. W. GRIFFITHS<sup>†</sup> AND G. O. HUGHES

Research School of Earth Sciences, The Australian National University, Canberra, ACT 0200, Australia

(Received 15 August 2009; revised 2 November 2009; accepted 2 November 2009)

Results of experimental and numerical studies are presented for a class of horizontal thermal convection in a long box forced at one horizontal boundary by two regions of destabilizing buoyancy flux separated by a region of stabilizing buoyancy flux. The steady-state circulation with zero net heat input is examined. The circulation generally involves two plumes, one at each end of the box, which drive overturning throughout the domain. The flow is classified into three regimes according to the pattern of interior circulation and depending on the relative heat input applied to the two destabilizing regions. Unequal heat inputs can double the interior stratification above that created by symmetric flow with two identical plumes, and when the heat inputs differ by more than 10%, the interior stratification is set by the stronger plume. The arrangement of boundary forcing broadly parallels the distribution of the zonally averaged surface cooling and heating in the Northern and Southern Hemispheres, and the results suggest that ocean overturning circulations may be sensitive to interhemispheric differences in the buoyancy inputs.

---

## 1. Introduction

The steady-state convection forced by heating and cooling at a single horizontal boundary has been studied for its fundamental significance as a form of convection having dynamics very different from Rayleigh–Bénard convection (Paparella & Young 2002; Mullarney, Griffiths & Hughes 2004; Wang & Huang 2005) as well as for its relevance to global ocean circulation (Rossby 1965, 1998; Hughes & Griffiths 2006). In most studies, the boundary conditions at either the top or bottom horizontal boundary of a box have been prescribed as a monotonic gradient of temperature from one end to the other, with all other boundaries insulating. In the steady-state, thermally equilibrated flow, there must be zero net heat input to the box. The flow consists of a narrow plume at one end of the box (adjacent to the boundary where the buoyancy input is destabilizing) and a broad relatively slow return flow towards the forcing boundary over the remainder of the box. Hence, the flow adjusts such that the thermal boundary layer gains just enough destabilizing buoyancy to drive it through the depth of the box despite a weak stable stratification throughout. When a sinusoidal temperature distribution (comprising a single cycle) is applied along the upper boundary such that the temperature is minimum at the midpoint (Paparella & Young 2002), the plume is located below this point and there is a circulation cell

<sup>†</sup> Email address for correspondence: Ross.Griffiths@anu.edu.au

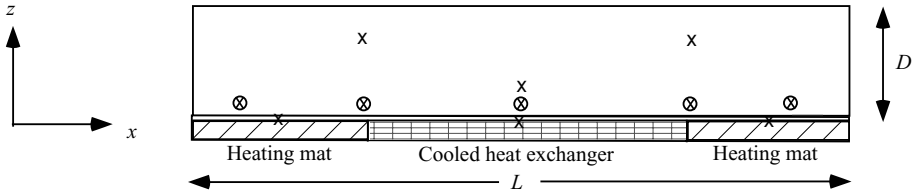


FIGURE 1. Side view of thermistor locations in the flow and the base of the tank. Those shown as  $\otimes$  were also used for vertical profiles through the depth.

on either side. Experiments and numerical solutions at substantially larger Rayleigh numbers, with heating over one end of the base and cooling over the other, reveal stability transitions within the horizontal thermal boundary layer and the vertical endwall plume, and also a large-amplitude low-frequency variability associated with eddies in the plume outflow (Mullarney *et al.* 2004; Hughes & Griffiths 2008).

The meridional overturning circulation of the oceans is forced at the ocean surface by a combination of buoyancy fluxes and wind stress. In a zonal average, surface waters are heated at low latitudes and cooled in both hemispheres at high latitudes, and heat is transported poleward. The overturning involves sinking of cold waters in small regions near both polar extremities and the sinking forms dense gravity currents, or plumes, on topographic slopes. On sinking the dense waters form, at least in the present day circulation of the Atlantic Ocean, large intrusions that fill the interior of the ocean with Antarctic Bottom Water (the densest water from the South) beneath North Atlantic Deep Water (slightly less dense water from the north). Thus, both northern and southern sinking currently contribute to the abyssal circulation (e.g. Schmitz 1995).

This paper examines the circulation maintained by differential thermal forcing applied along one horizontal boundary of a long box such that the supply of buoyancy is destabilizing near both ends and stabilizing near the centre. The study is stimulated by questions about the possible sensitivity of the deep ocean overturning circulation to the distribution of surface buoyancy (heat and freshwater) fluxes, but explores only a range of conditions practicable in the laboratory, and focuses on a simplified system without planetary rotation. The flow in general involves two plumes against the endwalls of the box, and the circulation is examined for its dependence on the difference between the two destabilizing buoyancy inputs. Sections 2 and 3 report laboratory experiments and §4 presents the results of computational simulations based on the laboratory configuration.

## 2. Experiments

### 2.1. Apparatus

Experiments were carried out in an acrylic tank of length  $L=1.25$  m, height  $D=0.20$  m and width  $W=0.15$  m (see figure 1) that was filled with de-aired water. The front and back sidewalls were double glazed, consisting of an inner wall that was 19 mm thick and an outer wall that was 3.5 mm thick. The gap was 18 mm wide and filled with Argon gas. The endwalls and the lid were 19 mm and 10 mm thick, respectively. Heat transfer with the surroundings was minimized by insulating with Styrofoam board, 45 mm thick on the sidewalls and 100 mm on the endwalls and the lid. The insulation on the sidewalls was temporarily removed during an experiment when taking temperature profiles and visualizing the flow.

---

Experiment	$H_1$ (W)	$H_2$ (W)	$R_Q$	$Ra_F$	$Pr$
2, 3, 15, 16	140	140	-0.0357	$3.58 \times 10^{14}$	5.10
4	139	141	-0.0286	$3.58 \times 10^{14}$	5.10
14	138	142	-0.0214	$3.58 \times 10^{14}$	5.10
5	137	142	-0.0179	$3.58 \times 10^{14}$	5.10
6, 13	135	145	0	$3.58 \times 10^{14}$	5.10
7, 12	130	150	0.0357	$3.58 \times 10^{14}$	5.10
8, 11	125	155	0.0714	$3.58 \times 10^{14}$	5.10
9, 10	115	165	0.143	$3.58 \times 10^{14}$	5.10
17, 30	156	154	-0.0422	$4.31 \times 10^{14}$	4.86
18, 19, 27, 29	158	152	-0.0551	$4.31 \times 10^{14}$	4.86
20, 26, 28	161	149	-0.0744	$4.31 \times 10^{14}$	4.86
21, 25	166	144	-0.107	$4.31 \times 10^{14}$	4.86
22, 24	171	139	-0.139	$4.31 \times 10^{14}$	4.86
23	181	129	-0.204	$4.31 \times 10^{14}$	4.86

---

TABLE 1. Summary of the relevant set of experiments. Experiment number is true to chronological order.  $H_1$  and  $H_2$  are the left- and right-hand heat inputs, and  $R_Q$  is the normalized difference in heating; see (2.2). The physical properties of water (see the caption to table 2) at the average interior temperature (33°C for experiments 2–16 and 35°C for experiments 17–30) were used to calculate flux Rayleigh number,  $Ra_F$ , and Prandtl number,  $Pr$  (see 2.1) for each experiment. When plotting the temperature gradient in figure 8, the data from experiments 17–30 were corrected for a calibration error in the power controller (the total heat input was 310 W instead of the desired 280 W, resulting in an increase in the average interior temperature and the top-to-bottom temperature difference). Temperature gradients were therefore rescaled, in order to compare all experiments, by a corrected top-to-bottom temperature difference  $\Delta T|_{max}(280 \text{ W}) = \Delta T|_{max}(310 \text{ W}) \times (280/310)^{5/6}$ ; see (3.2).

---

Forcing was applied at the bottom boundary rather than at the surface for practical reasons. Top and bottom forcing will be dynamically identical for a fluid having a linear equation of state and approximated as Boussinesq. (In addition, numerical solutions show that the flow is not significantly modified if the fluid is assigned the real properties of water under laboratory conditions similar to those used here; Mullarney *et al.* 2004). The tank base consisted of a 10 mm thick copper plate. One half of the copper plate, centred about the midpoint of the box length, formed part of a purpose-designed heat exchanger in which coolant water pumped through a maze of channels (0.63 m long) was in direct contact with the copper plate. The coolant was pumped from a water bath held at a fixed temperature of 16°C. The heat exchanger design and flow rate were chosen to ensure that the temperature of the copper over this half of the base was held as close to uniform as possible. The remaining half of the base area was heated by two electric resistance heating mats (each 0.30 m long and 0.15 m wide) pressed against the bottom of the copper plate at opposite ends of the box. Each heating mat delivered a heat flux that was constant and uniform over its area. Two different mat power controllers were used to set the heat flux. The first (thyristor-based) controller relied on an in-line power meter to measure the resultant power output (experiments 2–16; see table 1). However, voltage fluctuations in the mains supply were subsequently discovered to result in variations of up to 10 W in the actual delivered power. The second more sophisticated controller was purpose-designed to deliver a specified power within 0.1 W accuracy (experiments 17–30; see table 1).

The entire tank sat on a 100 mm thick Styrofoam layer on a wooden table top. There was an additional 40 mm of high temperature insulation under each heating mat. The sidewall double glazing and insulation enveloped the sides of the base heat exchanger and heating mats. The design of the apparatus and insulation is the same as that used by Mullarney *et al.* (2004), and we use their heat loss coefficient to estimate the heat loss from the insulated box as  $0.7425 \times (T_{\text{tank}} - T_{\text{lab}})$  (W), where  $T_{\text{tank}}$  is the average interior temperature in the box in steady state and  $T_{\text{lab}}$  is the ambient laboratory temperature. The total heat loss (as a percentage of the total heat input) in experiments 2–16 and 17–30 is found to be 2.7% and 2.2%, respectively.

Temperatures in the flow were measured using a set of eight thermistors, all fixed to a single traversing mechanism through small holes in the lid of the box. The thermistors were either held stationary to record temperature-time records or traversed downward to obtain vertical profiles of temperature. All were positioned close to the centreline of the box (figure 1). Five thermistors were at horizontal positions  $x/L = 0.08, 0.24, 0.5, 0.72$  and  $0.92$  and, when stationary, were at a distance  $z/D = 0.025$  above the base. These five also provided vertical profiles over the full depth of the box. The remaining three thermistors were used for time records alone (one at  $x/L = 0.5$ ,  $z/D = 0.15$ , and others at  $z/D = 0.85$ ,  $x/L = 0.24$  and  $0.72$ ). Additional three thermistors were embedded in the copper base at  $x/L = 0.25, 0.5$  and  $0.75$ .

## 2.2. Procedure

The approach of the flow to thermal equilibrium was monitored using a time series of the temperatures logged at 10 second intervals. Equilibration typically required five days and was judged to have been reached after the mean interior temperature had been stationary for at least one day. In this state the rate of heating (by the heating mats) was balanced by the sum of the rate of cooling (by the heat exchanger) and any heat loss to the room. The bulk temperature of the flow was controlled by the set cold plate temperature, whereas the vigour of convection was determined by the imposed power input. Once the flow was in thermal equilibrium, vertical temperature profiles were obtained at the five  $x$  positions shown in figure 1. Windowed-averages (based on individual measurements at 0.1 mm intervals) were used to remove bit-level measurement noise and construct profiles with a vertical resolution of 1.0 mm.

At the start of the series of experiments each heating mat was set to supply 140 W (i.e.  $F_T = 3111 \text{ W m}^{-2}$ ). In successive experiments, the heat input to one end of the base was increased while the power supplied to the other end was decreased by the same amount, thus keeping the total heat input into the tank constant. This was usually done without re-initializing the experiment from room temperature. After each adjustment of the forcing the experiment was left for about five days to reach thermal equilibrium before taking temperature profiles or flow visualization. The rationale for systematically increasing the heating difference (see (2.2)) to a maximum (positive) value, then decreasing it to a minimum (negative) value and finally returning to symmetric heating was to test for hysteresis in the system.

Flow visualization of the thermally equilibrated states was carried out using potassium permanganate crystals and neutrally buoyant food dye. The dye was introduced into the bottom boundary layer at strategic positions along the base via thin hypodermic tubes inserted through the endwalls of the box. Crystals of potassium permanganate were dropped through small ports in the lid to produce vertical dye lines, the subsequent distortion of which gave a qualitative picture of horizontal velocities. Digital video and high resolution still images were recorded.

### 2.3. Parameters

The parameters governing the flow are the aspect ratio  $A$ , the Prandtl number  $Pr$  and the flux-based Rayleigh number  $Ra_F$ , which we define as

$$A = \frac{D}{L}, \quad Pr = \frac{\nu}{\kappa}, \quad Ra_F = \frac{g\alpha F_T L^4}{\rho_0 c_p \kappa^2 \nu}, \quad (2.1)$$

respectively, along with the heating difference

$$R_Q^* = \frac{H_2 - H_1}{H_{tot}}. \quad (2.2)$$

Here,  $\nu$ ,  $\kappa$ ,  $\alpha$ ,  $c_p$  and  $\rho_0$  are the kinematic viscosity, thermal diffusivity, thermal expansion coefficient, specific heat capacity and a reference density of the fluid, respectively;  $g$  is the gravitational acceleration; and  $H_1$  and  $H_2$  are the rates of heat input (W) from the left and right heating mats, respectively.  $F_T$  is defined to be the average heat flux ( $\text{W m}^{-2}$ ) supplied by the heating mats, given by the total rate of heat input  $H_{tot} = H_1 + H_2$  divided by the total area of both heating mats.

When the heating mats at each end were set to supply equal power, the circulation was systematically biased in one direction. Neither the cause of this bias nor an internal flow mechanism to support asymmetry could be identified. We therefore apply a uniform correction to all  $R_Q^*$  values based on the imbalance between  $H_1$  and  $H_2$  required for the circulation to be symmetric about the centre of the box,

$$R_Q = R_Q^* - 0.0357. \quad (2.3)$$

The heating difference of interest to us,  $R_Q$ , then takes a value of zero when the flow was symmetric.

This study was designed to examine the sensitivity of the convective circulation to the heating difference  $R_Q$ . The thermal forcing was therefore kept fixed at a constant total heat input,  $H_{tot}$ , that was used in the previous work that examined heating at one end only, over a range of Rayleigh numbers (Mullarney *et al.* 2004). Only the heating ratio was varied systematically. The Rayleigh number was of order  $10^{14}$  (table 1) placing the flow in the high-Rayleigh-number ‘Entrainment regime’ described by Hughes & Griffiths (2008). Regarding the possible relevance to oceanic conditions (which are also expected to be in the Entrainment regime), the aim is to achieve dynamic similarity within the two-dimensional basin, non-rotating simplification and the constraints of the laboratory. One measure of the similarity, despite the oceanic Rayleigh number being much larger and aspect ratio much smaller than those achievable in the laboratory, is the depth of the thermal boundary layer relative to the water depth, which is approximately 0.1 in both cases. Another key measure is that the endwall plumes in the laboratory experiments are turbulent, as expected for dense slope plumes in the ocean.

## 3. Results

### 3.1. Qualitative observations

We classified the observed circulation into one of three regimes depending on the heating ratio  $R_Q$ . In all regimes, a similar flow was observed in the bottom boundary layer. Heating near the ends of the tank and cooling in the centre of the tank establishes temperature and pressure gradients along the base. Cold water in the bottom boundary layer flowed from the centre of the tank across the heated

portions of the base, gaining buoyancy and subsequently rising against the endwalls in unsteady, eddying plumes. A convective mixed layer was visible within the cold thermal boundary layer above each of the heated portions of the base, as observed by Mullarney *et al.* (2004). However, the convective mixed layers were thinner than those observed in the previous study, consistent with scaling theory that predicts the boundary-layer thickness to vary as the  $1/3$ -power of the length of the heated region (the total heat input and tank dimensions being the same).

### 3.1.1. Regime 1

For  $R_Q = 0$ , the flow was close to symmetric about  $x/L = 0.5$  (figure 2). Water in each plume rose through the full tank depth and formed an outflow along the upper boundary. The two outflows met near the midpoint of the box. The position of this confluence fluctuated by up to 0.1 m about the midpoint. There was some mixing at the confluence, but the bulk of the water from each plume outflow recirculated back to the same plume, either through entrainment into the plume or by first entering the bottom boundary layer.

### 3.1.2. Regime 2

For moderate values of  $R_Q$  ( $0.02 < |R_Q| < 0.1$ ) both plumes again penetrated through the full depth of the box and fed outflows along the upper boundary. However, the plume at the end with the larger applied heat input was stronger, having greater vertical velocities and a greater volume flux. The outflow from the stronger plume was more unsteady and had larger horizontal velocities. This outflow displaced the confluence towards the far end of the box (figure 3). A small amount of mixing was again evident at the confluence. Beneath the stronger outflow, water from both outflows was drawn towards the dominant plume while also moving downward towards the bottom boundary. Thus, circulation in the lower two-thirds of the tank depth consisted largely of a broad flow towards the stronger plume. Water was primarily either entrained into the stronger plume or entered the bottom boundary layer. Water that most recently passed through the weaker plume therefore filled a larger fraction of the interior than water most recently passed through the stronger plume.

### 3.1.3. Regime 3

For  $|R_Q| > 0.1$ , the stronger plume again dominated the overall circulation and under these conditions prevented the weaker plume from reaching the upper boundary (figure 4). The outflow from the dominant plume flowed along the upper boundary to the opposite end of the box, where it caused a downward motion against the endwall (as far as  $z/D = 0.25$  in the experiment shown). The weaker plume, not having enough buoyancy or momentum to force its way to the top, intruded into the interior above the boundary layer but below the height to which the stronger outflow descended. Throughout the interior below the stronger outflow there was a slow flow towards the dominant plume owing to entrainment into that plume and a slow downwelling into the bottom boundary layer.

## 3.2. Measurements of the flow

Several key aspects of the flow were measured, including the location  $x_c$  of the outflow confluence at the upper boundary, the penetration height  $z_{weak}$  of the weaker plume and the interior temperature gradient. The normalized, time-averaged position of the



FIGURE 2. Flow visualization of circulation in regime 1 for  $R_Q = 0$ . Neutrally buoyant food dyes, red and blue, were injected into the bottom boundary layer at  $x/L \sim 0.25$  and  $0.75$ , both starting at the same time. The dye was carried in the convective mixed layer towards the nearest endwall and then ascended in the endwall plumes. The time elapsed between the two photos was approximately 20 min. Although the insulation was removed from the tank sidewalls for only short periods during visualization, the dye seen at the top of the thermal boundary layer in the second frame was associated with downflow against the sidewalls due to the increase in heat loss from the tank during this period.

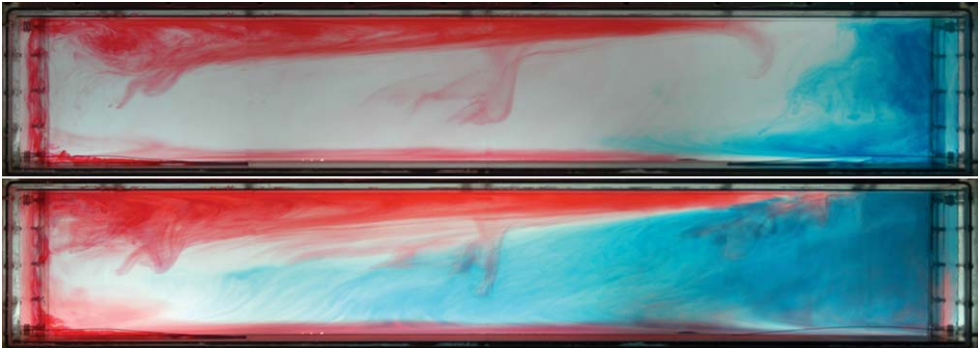


FIGURE 3. Flow visualization of circulation in regime 2 ( $0.02 < |R_Q| < 0.1$ ).  $R_Q = -0.07$ , left plume dominant. Neutrally buoyant food dye was injected into the bottom boundary layer at  $x/L \sim 0.25$  and  $0.75$ , the blue dye released on the right starting about 10 min before the red dye released on the left. The time elapsed between the two photos is approximately 20 min.



FIGURE 4. Flow visualization of circulation in regime 3.  $R_Q = -0.14$ , left plume dominant. The dye was injected as described for figure 3. Time elapsed between the two frames was approximately 13 min.

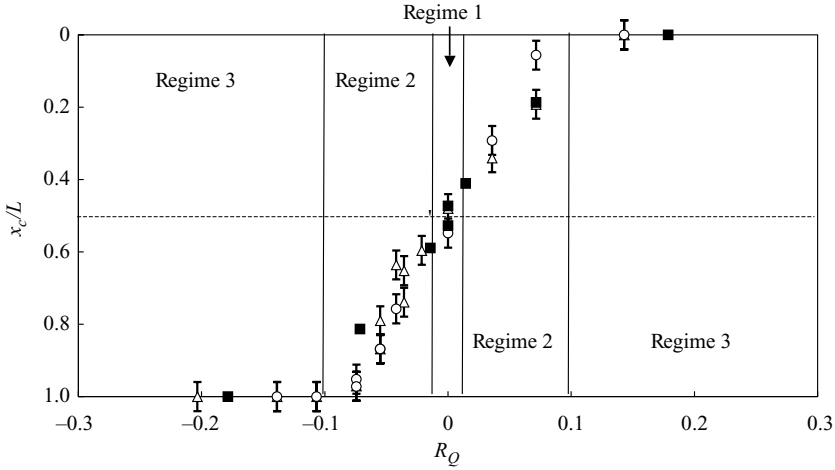


FIGURE 5. Normalized horizontal position of the confluence,  $x_c/L$ , as a function of the heating difference  $R_Q$ . Laboratory data for conditions attained in the sequence of increasing  $R_Q$  (experiments 6–9 and 24–30),  $\circ$ ; in the sequence of decreasing  $R_Q$  (experiments 10–23),  $\triangle$ ; numerical solutions,  $\blacksquare$ . Vertical lines indicate the flow regime boundaries.

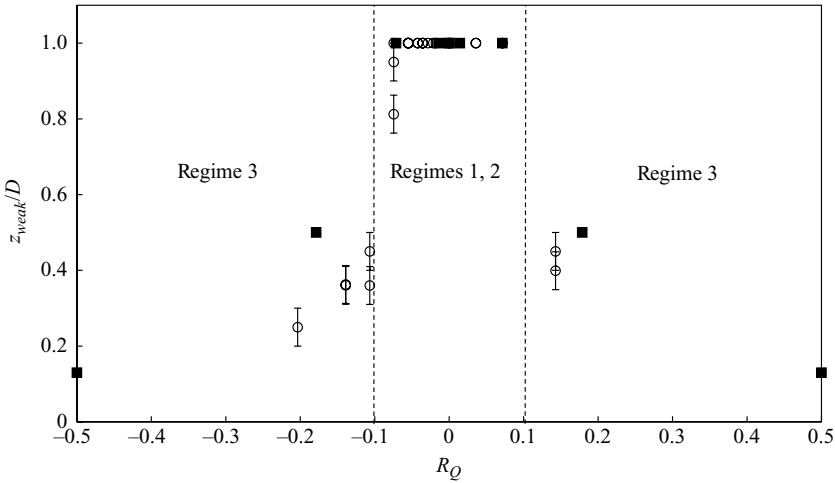


FIGURE 6. Penetration height of the weaker plume,  $z_{weak}/D$  as a function of forcing asymmetry  $R_Q$ . Experimental data,  $\circ$ ; numerical solutions,  $\blacksquare$ . The vertical dashed lines indicate the boundaries between regimes 2 and 3.

confluence,  $x_c/L$ , is plotted in figure 5 as a function of the heating difference. Where the outflow from the stronger plume reached the far endwall,  $x_c/L$  was recorded as either 0 or 1, depending on the sign of  $R_Q$ . The vertical bars in the plot indicate the observed range of  $x_c/L$  owing to time variation of the flow. The flow regime boundaries already defined above and based on the confluence position are also shown. In order to better explore regime 3, the penetration height of the weaker plume is plotted in figure 6 as a function of the heating asymmetry, where the vertical bars again indicate the extent of temporal variability.

The location of the confluence varied almost linearly with heating difference through regimes 1 and 2. In regime 3, the height of the weaker plume varied rapidly with

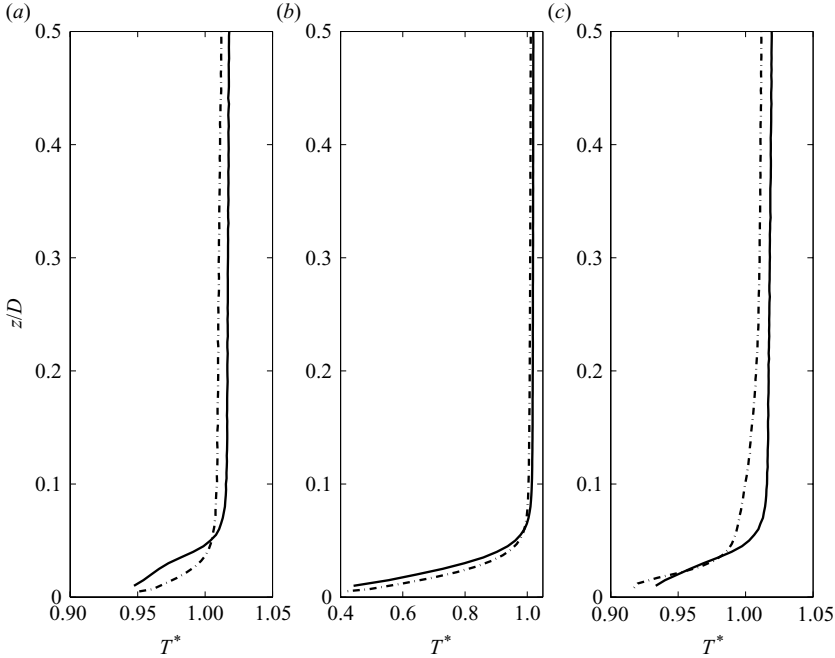


FIGURE 7. Normalized vertical profiles of temperature at  $x/L = 0.08$  (a), 0.5 and 0.92 (b,c) for experiments with  $R_Q = -0.04$  (solid line) and  $-0.20$  (dot-dashed line). Note the very different temperature scale in the centre frame.

heating difference for  $0.1 \leq |R_Q| \leq 0.2$  and approached  $z_{weak}/D \approx 0.13$  at  $|R_Q| \geq 0.5$ . The transition from regime 2 to regime 3 corresponds to change from a circulation in which both plumes entrain water over the full depth of the tank and set the stratification, to one in which the density structure is set by entrainment into the dominant plume and prevents the weaker plume from extending through the full depth of the tank (Wong & Griffiths 1999). Recalling that runs were carried out by stepping through a series of equilibrium states in both directions, we note that there is no evidence from figures 5 and 6 for the circulation to depend on previous conditions, and hence there is no hysteresis in the results.

Vertical profiles of temperature measured in two experiments are compared in figure 7. Here the temperature is normalized according to

$$T^* = \frac{T - T_c}{\overline{T_{1/2} - T_c}}, \quad (3.1)$$

where  $T$  is the measured temperature at any position,  $T_c$  is the temperature measured by the thermistor embedded in the centre of the cold plate and the denominator is a fixed value over all cases:  $\overline{T_{1/2} - T_c}$  is an averaged temperature difference between mid-height ( $z/D = 0.5$ ) and the cold plate for the symmetric case (based on the profiles taken at  $x/L = 0.5$  in all experiments with  $R_Q^* = 0$ ). Profiles are shown for the cases of almost symmetric heating and stronger heating at the left-hand end. The thermal boundary layer is easily identifiable in the profiles everywhere along the base in figure 7, which contrasts with the weakly stratified interior, where the gradient is barely visible on the temperature scale. Although the profiles from the two experiments are similar in many respects, there are significant differences. The profiles

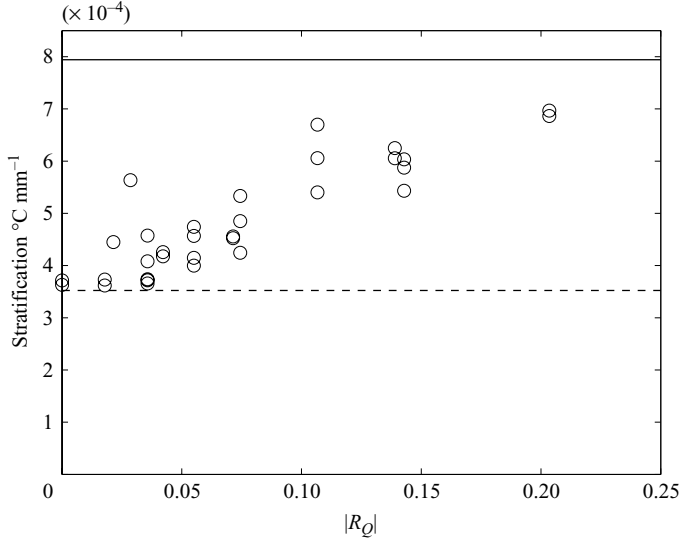


FIGURE 8. The interior stratification obtained from the experiments ( $\circ$ ) as a function of  $|R_Q|$ . The scaled laboratory data from Mullarney *et al.* (2004) for  $R_Q = 1$  and 0 are represented by the solid and dashed lines, respectively. The comparison at  $|R_Q| = 1$  requires a small adjustment to relate the stratification measured by Mullarney *et al.* (2004) for 271 W heat input, to the present case having 280 W heat input: a 3% larger heat input implies a 2.7% larger stratification (Hughes *et al.* 2007).

for  $R_Q = -0.2$  show the boundary layer to be warmer at  $x/L = 0.08$  and colder at  $x/L = 0.92$ , reflecting the greater heat input at the left-hand end. With this asymmetric forcing there is also a slight horizontal gradient of the same sign in the interior (not visible in figure 7). The interior vertical gradient for  $R_Q = -0.2$  is also significantly increased above the boundary layer at  $x/L = 0.92$  by the intruding outflow from the weaker plume. On the left, there is a thinning of the boundary layer above the more strongly heated base.

The vertical profiles measured in the centre of the tank have been used to calculate the interior temperature gradient (figure 8) from a linear fit between  $0.4 \leq z/D \leq 0.7$ . The stratification doubled between  $|R_Q| = 0$  and  $|R_Q| = 0.2$ . We do not expect further significant increases in stratification at larger  $|R_Q|$  because in regime 3 the density field is set by the dominant plume (Wong & Griffiths 1999). The results can be compared with the case of a single heated region, as in the experiments of Mullarney *et al.* (2004) (even though their bottom boundary condition—imposed input heating flux over the left half and imposed cooling temperature over the right half of the base—is not strictly the same as for the  $|R_Q| = 1$  limit of the present study, in which the total heat input is supplied through one quarter of the base). This value ( $7.9 \times 10^{-4} \text{ } ^\circ\text{C mm}^{-1}$ ) for  $|R_Q| \equiv 1$  is shown in figure 8 and is consistent with the trend of the data.

When  $R_Q = 0$  the heat input to each plume was 140 W and the circulation was approximately symmetric about the centre of the box. Thus, it is instructive to compare this case with the case of a single plume forced by a 140 W input as previously reported by Mullarney *et al.* (2004): in that case the circulation resembled one of the two overturning cells in our  $R_Q = 0$  experiment, but with twice the horizontal scale, and the interior stratification was measured to be  $4.4 \times 10^{-4} \text{ } ^\circ\text{C mm}^{-1}$ . If we assume that the stratification  $dT/dz \sim \Delta T|_{max}/D$ , the scaling of Hughes *et al.* (2007) (their

equation (4.3)) suggests that

$$D \frac{dT}{dz} \sim \Delta T|_{max} \sim \ell^{1/3} H_{tot}^{5/6}, \quad (3.2)$$

where  $\Delta T|_{max}$  is the top-to-bottom temperature difference and  $\ell$  is the horizontal length scale characterizing the overturning cell. Therefore, halving the horizontal scale of an overturning cell will reduce the top-to-bottom density difference by a factor of  $2^{1/3}$ : we expect the interior stratification in our experiments at  $R_Q = 0$  to be  $3.5 \times 10^{-4} \text{ }^\circ\text{C mm}^{-1}$  (dashed line in figure 8), and this indeed forms a lower bound to the stratification at all values of  $R_Q$ . For a given total heat input the interior stratification is larger (by up to approximately two times) for greater asymmetry in the forcing, and (3.2) helps identify the causes of this increase. As the destabilizing buoyancy is divided into multiple ( $n$ ) regions, the reduction in horizontal length scale characterizing each cell tends to decrease the stratification (by a factor  $n^{1/3}$  when all plumes are equal) because more plumes result in greater interior flushing. A further reduction in stratification (by a factor  $n^{5/6}$  when all plumes are equal) occurs because the buoyancy input into each plume is reduced. Figure 8 shows that if the strengths of individual plumes differ by only a small amount ( $\sim 10\%$  for two plumes), the stratification is determined by the buoyancy flux in the strongest plume.

## 4. Numerical solutions

### 4.1. Computational details

The two-dimensional momentum, continuity and heat equations were solved numerically using the computational fluid dynamics package FLUENT. The computations used a finite-volume method and flow was allowed to be fully non-hydrostatic but incompressible and Boussinesq. (In FLUENT we used the two-dimensional implicit segregated solver with the ‘PRESTO!’ interpolation scheme for pressure, the ‘PISO’ algorithm for pressure–velocity coupling and the ‘QUICK’ scheme for discretization of the momentum and energy equations.) A turbulence closure model was not required because the Kolmogorov scales were resolved explicitly. The working fluid was assumed to be water, for which the density–temperature relation was linearized and the properties ( $\kappa$ ,  $\nu$ ,  $\rho_0$ ,  $c_p$ ,  $\alpha$ ) evaluated at the average interior temperature measured in the corresponding laboratory experiment having the same thermal forcing conditions. All boundaries were no-slip and the top boundary and endwalls were perfectly insulating. The bottom boundary conditions for runs 1–8 consisted of an imposed temperature of  $16^\circ\text{C}$  at  $0.25 \leq x/L \leq 0.75$  and prescribed, uniform heat fluxes through one-quarter of the base at each end of the box.

The computational domain was given the same overall dimensions as the laboratory tank ( $0.20 \text{ m} \times 1.25 \text{ m}$ ) and consisted of interior cells  $0.01 \text{ m} \times 0.01 \text{ m}$  surrounded by regions of finer mesh adjacent to all boundaries. In the finer mesh adjacent to each horizontal boundary, there were 12 rows of cells, the height of successive rows increasing in a geometric fashion (by a factor of 1.3) from  $5 \times 10^{-4} \text{ m}$  for the first row against the boundary. The total thickness of each of these high resolution regions was therefore  $0.037 \text{ m}$  ( $z/D = 0.19$ ). Adjacent to each vertical endwall there were 32 columns of cells, the width of successive columns increasing in a geometric fashion (by a factor of 1.015) from  $1 \times 10^{-3} \text{ m}$  for the first column at the boundary. The total width of each of these high-resolution endwall regions was therefore  $0.041 \text{ m}$  ( $x/L = 0.03$ ). This computational grid was chosen after trial solutions with a range of mesh resolutions and represents the lowest resolution for which solutions

---

Run	$H_1$ (W)	$H_2$ (W)	$R_Q$
1	140	140	0
2	142	138	-0.014
3	150	130	-0.071
4	165	115	-0.179
5	175	105	-0.250
6	210	70	-0.500
7	245	35	-0.750
8	280	0	-1
9	280	—	—

---

TABLE 2. Parameters used in the numerical simulations. All runs had an equivalent total heat input  $H_{tot} = 280$  W. The properties of water were evaluated at the steady-state interior temperature measured in experiments 2–16 (33°C, and constant over the range of  $R_Q$ ):  $\rho = 994.74 \text{ kg m}^{-3}$ ,  $\alpha = 3.282 \times 10^{-4} \text{ K}^{-1}$ ,  $\nu = 7.535 \times 10^{-7} \text{ m}^2 \text{ s}^{-1}$ ,  $\kappa = 1.477 \times 10^{-7} \text{ m}^2 \text{ s}^{-1}$  and  $c_p = 4177.54 \text{ J kg}^{-1} \text{ K}^{-1}$ . Thus, all runs had  $Ra_F = 3.58 \times 10^{14}$  and  $Pr = 5.1$ .

---

demonstrated grid-independence (as judged on the basis of the time-averaged values of key quantities characterizing the circulation). In particular, it was found to be important to resolve the flow of narrow horizontal extent at the base of the endwall plumes.

The external parameters examined in a series of nine numerical simulations are given in table 2. The Rayleigh and Prandtl numbers were chosen to match those in the first series of laboratory experiments. Likewise, the thermal boundary conditions for the first four simulations were chosen to match four of the laboratory experiments, with heating differences spanning the three regimes defined in § 3.1. Runs 5–8 extend the range of heating differences beyond those examined in the experiments (to  $|R_Q| = 0.25, 0.5, 0.75$  and 1). In run 8, all of the heat input was applied through the left quarter of the base, resulting in a circulation containing just one plume. Run 9 is used to compare our results with those of Mullarney *et al.* (2004): we fixed the temperature on the right *half* of the base at 16°C and imposed a uniform flux over the left *half* to give a heat input (equivalent to that in the 150 mm wide experimental apparatus) of 280 W. A comparison of runs 8 and 9 allowed an assessment of the sensitivity of the convection to this detail in the distribution of base heating.

In run 1 the flow fields were initialized as stationary and isothermal at room temperature and allowed to adjust and thermally equilibrate to the boundary conditions by stepping forward in time (a 0.25 s step was used in all runs). Subsequent runs were initiated from the equilibrated solution in run 1 and allowed to re-equilibrate to the different boundary conditions. In each case, the flow was judged to be in equilibrium once the rate of heat removal from the cooled sections of the base matched the heat input into the box to within 0.5 % (which typically required 24 hr of simulated flow time). The simulation was then continued after this stage for 5–10 hr (simulated flow time) in order to obtain a record of low-frequency variability in the steady-state flow.

#### 4.2. Results

An example of the computed stream function, velocity and temperature fields at one instant after the flow had reached thermal equilibrium for the symmetrically forced case ( $R_Q = 0$ ) is shown in figure 9. However, an animation of a time sequence of solutions highlights marked variability in the equilibrated flow. The variability includes

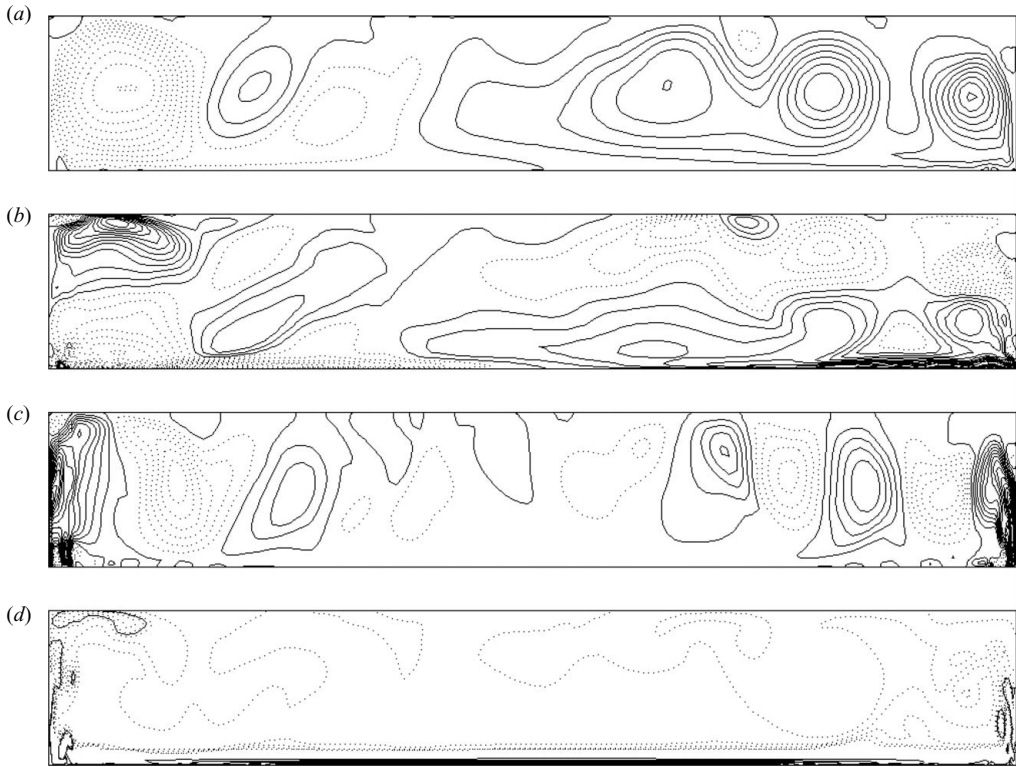


FIGURE 9. Examples of instantaneous flow fields for the numerical simulation with  $R_Q = 0$ : (a) stream function (per unit spanwise width,  $\text{m}^2 \text{s}^{-1}$ ), (b) horizontal velocity ( $\text{m s}^{-1}$ ), (c) vertical velocity ( $\text{m s}^{-1}$ ) and (d) temperature. In (a–c), solid lines show positive and zero contours and dotted lines show negative contours. The contour intervals are  $2 \times 10^{-5} \text{m}^2 \text{s}^{-1}$  in (a) and  $0.5 \text{mm s}^{-1}$  in (b) and (c). In (d), the solid contour intervals are  $3^\circ\text{C}$  and the dotted contour interval is  $0.01^\circ\text{C}$  (over the range  $46.77^\circ\text{C}$  to  $46.87^\circ\text{C}$ ).

displacement and evolution of coherent eddies and fluctuation in the confluence location. For example, a train of alternately signed disturbances appear in the thermal boundary layer at the base (figure 9c, d) and travel towards the plume. These are analogous to instabilities in the convective mixed layer observed in the laboratory experiments, but in the computed solutions they are forced to be two-dimensional in the cross-stream direction rather than having the streamwise orientation preferred in the experiments. Large amplitude disturbances also form in the endwall plumes and travel up to the top of the box. Eddies of larger scale form where the plumes feed the outflows and these travel slowly away from the endwalls, giving large variability at low frequencies. In these two-dimensional solutions entrainment into the endwall plumes may behave differently to the laboratory experiments, where flow becomes three-dimensional. Nevertheless, we find that the stratification increases by a factor of approximately two as  $|R_Q|$  is increased from 0 to 0.179, which compares well with the laboratory results.

Time-averaged flow fields were constructed by averaging 3600 instantaneous solutions (at 5 s intervals over 5 hr), as shown (for  $R_Q = 0$ ) in figure 10. The case having symmetric forcing exhibits a high degree of symmetry in the mean flow. In particular, the plume outflows meet at the midpoint of the box. As the heating

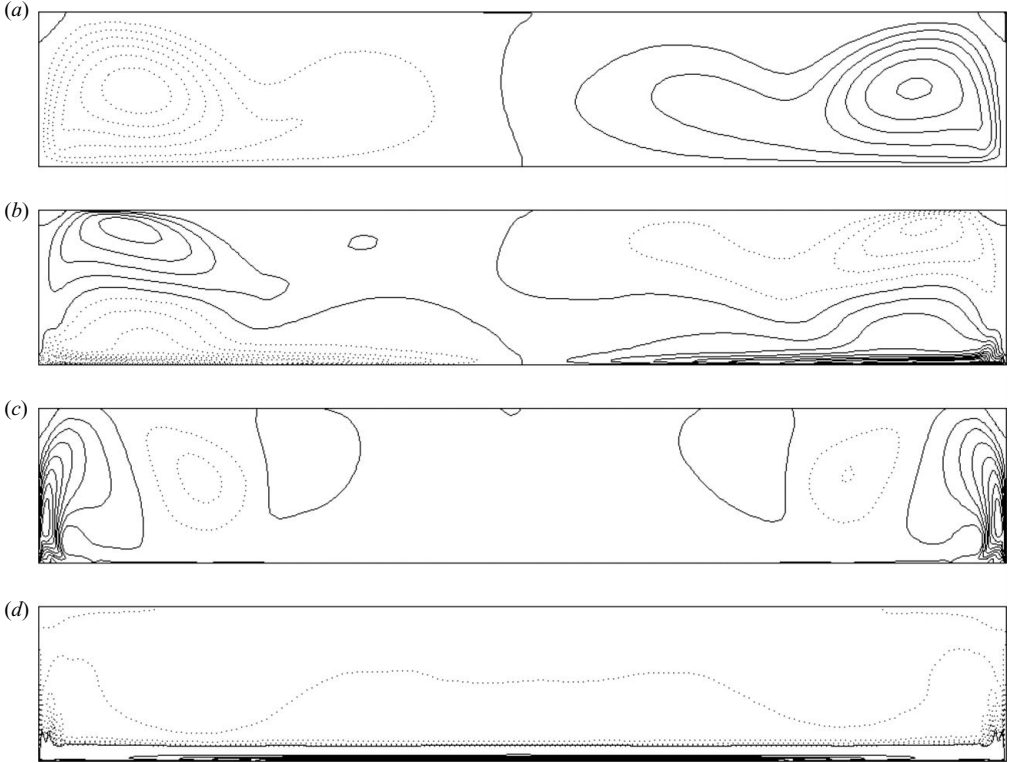


FIGURE 10. Example of time-averaged flow fields for the numerical simulation with  $R_Q = 0$ : (a) stream function (per unit spanwise width,  $\text{m}^2 \text{s}^{-1}$ ), (b) horizontal velocity ( $\text{m s}^{-1}$ ), (c) vertical velocity ( $\text{m s}^{-1}$ ) and (d) temperature. In (a–c), solid lines show positive and zero contours and dotted lines show negative contours. The contour intervals are  $2 \times 10^{-5} \text{m}^2 \text{s}^{-1}$  in (a) and  $0.5 \text{mm s}^{-1}$  in (b) and (c). In (d), the solid contour interval is  $3^\circ \text{C}$  and the dotted contour interval is  $0.01^\circ \text{C}$  (over the range  $46.84^\circ \text{C}$  to  $46.94^\circ \text{C}$ ).

difference is increased, one plume becomes increasingly dominant, as is apparent in the stream functions shown in figure 11. The outflow from the stronger plume extends further along the top of the box as  $|R_Q|$  is increased, and the two overturning cells of opposite sign become increasingly asymmetric. For  $|R_Q| \sim 0.179$ , the circulation consists mainly of a single cell. In all cases, the stronger plume penetrates the full depth of the box and its outflow occupies almost half the depth of the box. Hence, the outflow is slightly thicker than that observed in the experiments.

The vertical velocity (figures 9c and 10c) reveals the presence of a weak downwelling region outside each of the plumes. The downwelling near the stronger plume increases in strength with increasing forcing asymmetry (figure 11), and the downward deflection of isotherms near  $x/L = 0.16$  (figures 9d and 10d) is increased. A region of circulation of opposite sign (figure 11c,d) and a reversal in horizontal velocity appear near the upper boundary at  $x/L = 0.24$ .

Figure 12 shows vertical profiles of time-averaged horizontal velocity  $u$  at three locations along the box and as a function of forcing asymmetry. The profiles for  $R_Q = 0$  are consistent with a velocity field that is approximately antisymmetric about the tank's midpoint. This structure bears some similarities with the antisymmetric first-order horizontal velocity field observed in experiments with an identical turbulent

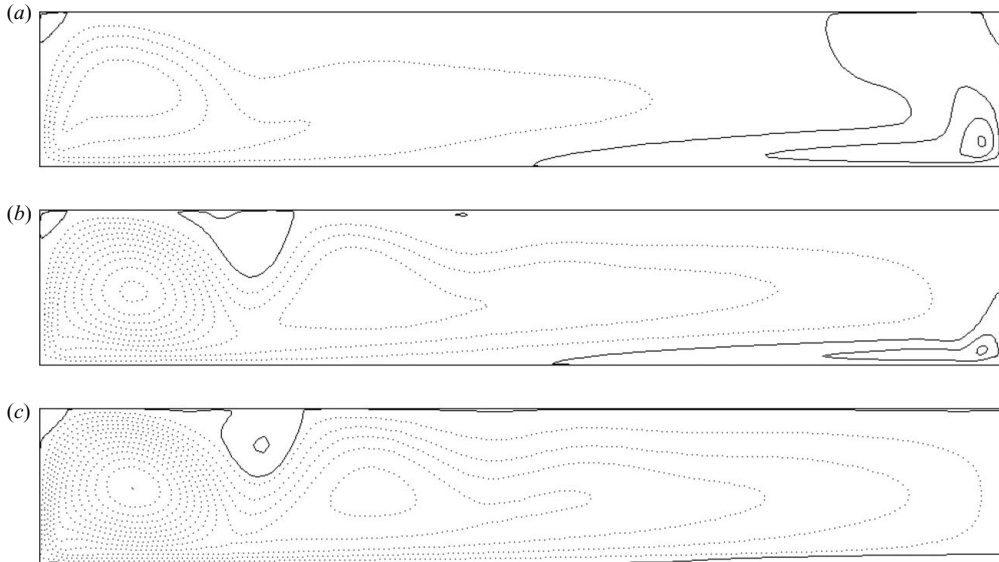


FIGURE 11. Time-averaged stream function (per unit spanwise width,  $\text{m}^2 \text{s}^{-1}$ ) for (a)  $R_Q = -0.014$ , (b)  $R_Q = -0.179$  and (c)  $R_Q = -1$ . The solid lines show positive (counterclockwise flow) and zero contours, and dotted lines show negative contours; the contour interval is  $2 \times 10^{-5} \text{m}^2 \text{s}^{-1}$ . The time average is based on 5 hr of the thermally equilibrated numerical simulation.

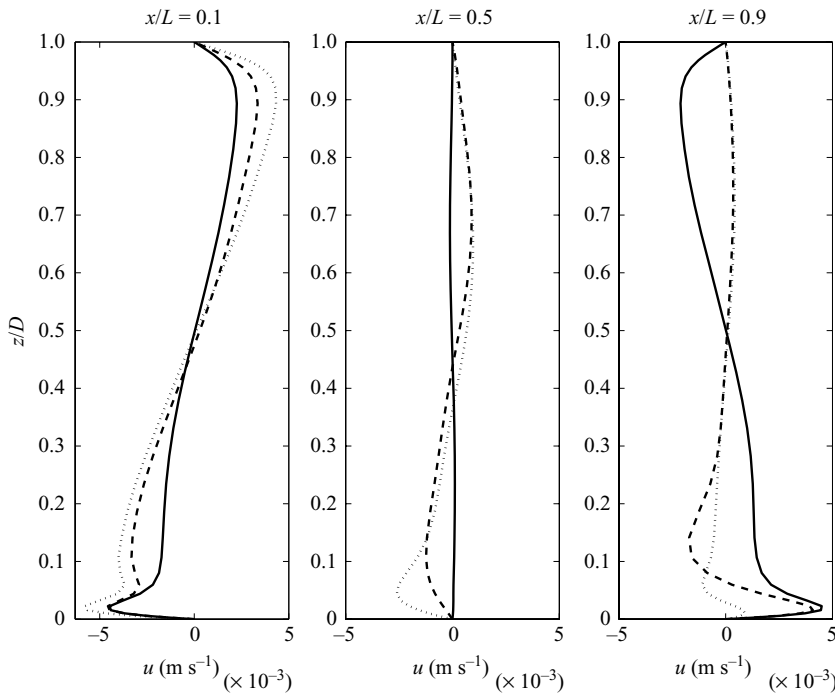


FIGURE 12. Vertical profiles of time-averaged horizontal velocity at  $x/L = 0.1, 0.5$  and  $0.9$  for  $R_Q = 0$  (solid line),  $R_Q = -0.179$  (dashed line) and  $R_Q = -1$  (dotted line).

plume maintained at each end of a box (Griffiths & Bidokhti 2008) and fed from external reservoirs, thus supplying a net buoyancy input. In that case, the plumes drive a mean filling-box circulation with superposed internal waves, which, in turn, generate quasi-horizontal shear layers similar to those driven by a single turbulent plume in the filling-box circulation (Wong, Griffiths & Hughes 2001). The present problem of horizontal convection with zero net heat input maintains a very different density stratification and numerous horizontal shear layers are not evident.

In contrast to the symmetric case, the profiles for  $R_Q = -0.179$  and  $R_Q = -1$  illustrate the circulation in regime 3, for which there is a dominant plume at the left end and a single strong outflow near the top of the box. The bottom boundary layer is drawn strongly towards the dominant plume along much of the box length. In addition, entrainment into the dominant plume draws water to the left throughout most of the lower half of the box. These aspects of the circulation associated with the plume strengthen as  $|R_Q|$  increases. Two other features in the profiles at  $x/L = 0.9$  are also worthy of note: The intrusion formed by the weaker plume for  $R_Q = -0.179$  occurs at depths  $0.1 < z/D < 0.2$ , and a weak cell (whose sense is consistent with buoyancy forcing in the presence of diffusion over the insulated region of the base and with external stress) appears against the right end of the base for  $R_Q = -1$ .

A comparison between the present results for  $R_Q = -1$  (run 8), the solutions of Mullarney *et al.* (2004) and the present equivalent case (run 9), revealed an overall consistency of the flow fields. Mullarney *et al.* (2004) reported a small and shallow intrusion from the base of the rising plume that was not observed at the steady state in either run 8 or run 9. However, these solutions were obtained with a finer mesh along all the boundaries and a more stringent criterion for approach to thermal equilibrium.

## 5. Analysis of the results

The confluence position  $x_c$  and the penetration height of the weaker plume  $z_{weak}$  were found from the computed flow solutions for horizontal velocity and vertical velocity, respectively. The results are shown in figures 5 and 6 for comparison with the laboratory measurements. The simulations and experimental results are in good agreement, although the measured penetration height of the weaker plume for  $|R_Q| \sim 0.2$  was a little smaller in the experiments than that computed. The agreement indicates that the three dimensionality and small scales in the laboratory experiments do not in themselves substantially affect the large-scale flow and that entrainment into the endwall plumes is approximately captured in the numerical solutions. The small difference in the plume penetration height is likely to be accounted for by a stronger stratification due to sidewall heat loss in the laboratory. A general conclusion is that a difference of only 10% or greater in the power supplied to the two heated regions again resulted in the stronger plume dominating the circulation.

The magnitude of the stream function extremum near each end of the box provides a measure of the vertical mass transport associated with each plume. The ratio of the overturning rate associated with the weak plume ( $|\psi_{weak}|$ ) to that associated with the dominant plume ( $|\psi_{dom}|$ ) is plotted in figure 13(a) as a function of  $|R_Q|$ . The two cells are of similar strength when  $R_Q = 0$ , as expected, whereas one cell dominates the other when the forcing is even slightly asymmetric, and vertical transport in the weak cell becomes insignificant for  $|R_Q| > 0.5$ . The strong nonlinearity in the ratio of the two mass transports reflects the differing height of penetration of the weaker plume, the differing entrainment into the plume from the interior, and differing extent to

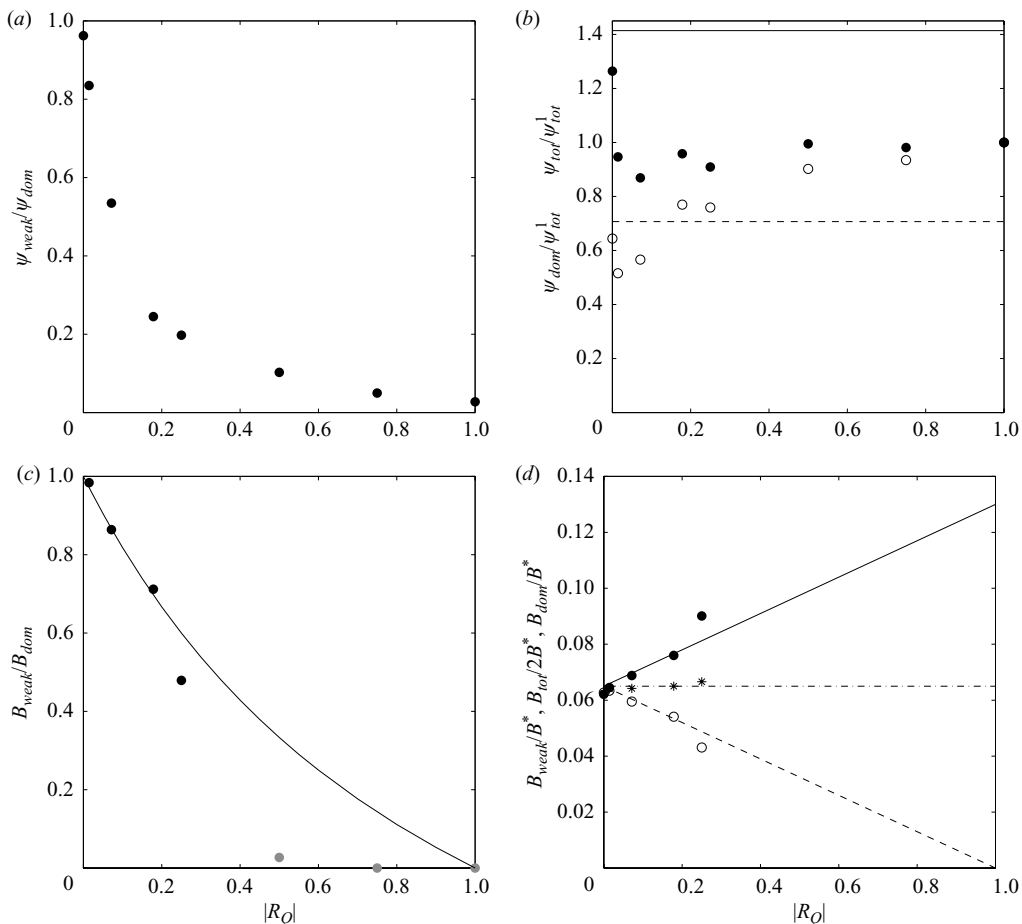


FIGURE 13. The relative strengths of plumes and overturning in the computed solutions, measured by (a) the ratio of plume stream functions, (b) the stream functions relative to that for the single plume case  $\psi_{tot}/\psi_{tot}^1$  (solid circle) and  $\psi_{dom}/\psi_{tot}^1$  (open circle), (c) the ratio of plume buoyancy fluxes, and (d) the ratios of individual plume buoyancy fluxes to the total flux  $B^*$  (dominant plume, solid circles; weak plume, open circles) all as functions of  $|R_Q|$ . Included in (b) are the upper bound for  $\psi_{tot}/\psi_{tot}^1$  (solid line) and the scaling prediction for  $\psi_{dom}/\psi_{tot}^1$  (dashed line), both of which are expected to be relevant at  $R_Q=0$ . The curve in (c) is the theoretical prediction (5.3). The solid and dashed lines in (d) are the prediction (5.3). Also shown in (d) is the ratio of the computed sum of the two plume buoyancy fluxes to the total flux (stars) and theoretical prediction  $B_{tot}=0.13B^*$  (dash-dotted line).

which the plumes capture water from the bottom boundary layer. The mass transport in the dominant plume and the total overturning rate  $\psi_{tot}$  ( $=|\psi_{weak}|+|\psi_{dom}|$ ) in the box are shown in figure 13(b), where they are normalized by  $|\psi_{tot}^1|$ , the mass transport for the single plume case ( $|R_Q|=1$ ) and the same heat input. In this plot,  $|\psi_{dom}|=\psi_{tot}=|\psi_{tot}^1|$  at  $|R_Q|=1$ . There is a minimum total vertical transport near  $|R_Q|\approx 0.1$ , a minimum individual (dominant) plume transport near  $|R_Q|\approx 0.01$  and the maximum total transport occurs in the symmetric case  $R_Q=0$ .

The data in figure 13(b) can be compared with predictions of a theoretical model of steady-state horizontal convection based on turbulent plumes (Hughes & Griffiths 2008). When there are multiple plumes (with a given total heat throughput), the

stream function is predicted to satisfy

$$\frac{\overline{|\psi_{max}|}}{|\psi_{tot}^1|} \sim n^{-1/2}, \quad \frac{|\psi_{tot}^n|}{|\psi_{tot}^1|} \leq n^{1/2}, \quad (5.1)$$

where  $|\psi_{tot}^n|$  is the total overturning rate with  $n$  half line-plumes in the box (a half plume being one that can entrain on only one side), and  $\overline{|\psi_{max}|}$  is the mean rate of overturning taken over  $n$  circulation cells associated with the  $n$  half plumes, which is equal to  $\psi_{tot}/n$ . For  $n=2$ , the case of two endwall plumes, this gives  $\overline{|\psi_{max}|}/|\psi_{tot}^1| \approx 0.71$ ,  $|\psi_{tot}^n|/|\psi_{tot}^1| \leq 1.4$  and  $\overline{|\psi_{max}|} = |\psi_{tot}|/2$ . Note that two plumes of equal strength will be able to entrain more interior fluid than two plumes of unequal strength because the surface area over which entrainment of interior fluid can occur is maximized. Thus, the largest total overturning rate in figure 13, approximately 90 % of the predicted upper bound, is achieved for two equal strength endwall plumes. Hence, the scaling predictions are roundly consistent with the computations and provide good estimates in the case of two equal plumes. As  $R_Q$  is increased from zero, both the total overturning rate and the transport in the dominant plume decrease sharply towards a minimum at  $|R_Q| \approx 0.1$ , where the transition between regimes 2 and 3 was observed in the experiments. Moving to values of  $|R_Q|$  larger than this, where one plume strongly dominates the overall circulation, the total overturning rate increases until, as  $|R_Q|$  approaches 1, the overturning approaches that commensurate with a single endwall plume in the same box.

The buoyancy fluxes (per unit spanwise width,  $\text{kg s}^{-3}$ ) carried by the plumes are a function of height. However, useful comparisons are obtained by evaluating the buoyancy fluxes at the upper edge of the cold bottom boundary layer according to

$$B_1 = g\rho_0\alpha \overline{\int_0^{L_1} w(T - T_h) dx}, \quad B_2 = g\rho_0\alpha \overline{\int_{L_2}^L w(T - T_h) dx}, \quad (5.2)$$

where  $B_1$  and  $B_2$  are the time-averaged buoyancy fluxes for the left and right endwall plumes, respectively,  $w$  is the vertical velocity,  $T_h$  is a temperature at the top of the boundary layer evaluated by taking a horizontal average of the temperature field (along the length of the box, between the plume edges) at the height  $h$ , and the overbar on the integrals denotes a time average (based on 7200 fields over 10.5 hr of simulation). At each solution time step during this period, the boundary layer depth  $h$  was calculated by finding the maximum temperature difference  $T_{max} - T_{min}$  for every grid column above the cooled region of the bottom boundary, the height above the base that accommodates 95 % of this difference, and then taking the average over the region. The edges of the left and right endwall plumes (at  $x = L_1$  and  $x = L_2$ , respectively) were defined to be where the relevant integral in (5.2) reached a maximum as  $L_1$  was increased from zero or as  $L_2$  was decreased from  $L$ , respectively.

Figure 13(c) shows the ratio of the computed time-averaged buoyancy fluxes in two plumes. The results can again be interpreted using the turbulent plume model for horizontal convection (Hughes *et al.* 2007), which predicts (for a single plume) that the buoyancy transport at the edge of the thermal boundary layer (at  $z = \delta_{0.95}$ , again the height encompassing 95 % of the top-to-bottom temperature difference) will be 14 % of the total buoyancy input  $B^*$  at the base. If we assume that this result can be extended to the case of multiple plumes and that the buoyancy flux to the base of each plume is that provided by the respective heated region (heat input  $H_1$  or  $H_2$ ),

then we can write

$$B_{dom} = c(1 + |R_Q|) \left( \frac{B_{tot}}{2} \right), \quad B_{weak} = c(1 - |R_Q|) \left( \frac{B_{tot}}{2} \right),$$

$$\frac{B_{weak}}{B_{dom}} = \frac{1 - |R_Q|}{1 + |R_Q|}, \quad (5.3)$$

where  $B_{dom} + B_{weak} = B_{tot} = cB^*$  and  $c$  is an unknown constant. These predictions are shown in figures 13(c) and 13(d) for  $c = 0.13$  and provide a reasonable description of the results from the computed solutions for  $|R_Q| < 0.25$ , including the nonlinearity in the plume flux ratio as a function of  $|R_Q|$ . The agreement of this best-fit value of  $c$  with the theoretical value from a single plume model (14 %) supports the application of the theoretical model to the range of cases from equal to moderately unequal plumes.

For  $|R_Q| > 0.25$  a horizontal temperature gradient is observed to develop at the height  $z = \delta_{0.95}$ , making a reliable definition of the boundary layer difficult. Moreover, as the weaker plume outflow is confined to the region immediately above the boundary layer, the calculation of the buoyancy fluxes (5.2) is prone to errors. The three data points most affected are shown in figure 13(c) in grey, and for clarity are omitted in figure 13(d). We observe that the dividing streamline separating the two circulation cells in figure 11 meets the base farther to the right of the midpoint as  $R_Q$  becomes more negative. Hence, we suggest that the position of the dividing streamline is such that the supply and removal of buoyancy is in approximate balance within each cell.

## 6. Conclusions

The key result in this study is that the relative transport in the two plumes is sensitive to small departures from symmetry in the destabilizing buoyancy input, and one plume dominates the circulation for input differences of 10 % or greater. The circulation patterns for asymmetric forcing involve a larger full-depth overturning cell and a smaller cell occupying only a fraction of the depth of the box. Over a range of asymmetry (regimes 2 and 3,  $|R_Q| \sim 0.1 - 0.2$ ) the dominant plume draws water from more than half of the horizontal thermal boundary layer and entrains more of the interior than the weaker plume, thus drawing water that has most recently passed through the weaker plume across the interior of the box. Tracer from the weaker plume therefore quickly fills much of the interior. These features are reminiscent of the northward penetration of the Antarctic Bottom Water into the North Atlantic basin and the spreading of North Atlantic Deep Water from the northern boundary, at mid-depth throughout the Atlantic Ocean.

The line plumes in our experiments, and even more so in the two-dimensional numerical solutions, are far from the turbulent slope currents that carry deep and bottom waters to large depths in the Southern Ocean and the North Atlantic Ocean. There should be no pretence that such a simple rectangular and non-rotating model will yield the same (normalized) stratification as that in the oceans. In the present two-dimensional geometry, the strongest interior stratification (when normalized by the top-to-bottom temperature difference divided by the depth of the box) is 20 times smaller than that measured in the abyssal oceans, and the thermocline thickness calculated by applying the two-dimensional model to the ocean is much smaller than that observed in the ocean. This is not surprising, however, because the difference between a line plume and an axisymmetric plume has a substantial influence on the predicted density profile (Hughes *et al.* 2007). The more highly localized sinking

from a three-dimensional ‘point’ source is predicted to lead to a greater interior stratification, along with a larger and more realistic ocean thermocline thickness. The dynamics of geostrophic currents on a slope must also be taken into account.

The aim in this paper has been to examine the dynamics of the circulation with two sinking regions in a simple case that provides insights relevant to more general cases. The choice of imposed heat inputs enables us to measure both temperatures and fluxes; ostensibly similar behaviour is expected for other types of boundary conditions that lead to a heat transport. The results show that for a given total rate of buoyancy forcing, the interior stratification in the two-dimensional basin with one line plume can be greater by up to a factor of two compared with that generated by two line plumes, and the weakest possible interior stratification occurs when the buoyancy input is divided between two identical destabilizing regions. Equivalently, for a given individual plume flux, two plumes give approximately  $\sqrt{2}$  times the stratification of a single plume case. These results are consistent with theoretical solutions (Hughes *et al.* 2007) for plumes of equal strength, but highlight further questions regarding modelling the interaction of multiple plumes of unequal strength.

We thank Tony Beasley for assistance with the laboratory experiments. The work was partly funded by the Australian Research Council (DP0664115), and the numerical simulations were supported by an award under the Merit Allocation Scheme on the NCI National Facility at The Australian National University.

#### REFERENCES

- GRIFFITHS, R. W. & BIDOKHTI, A. A. 2008 Interleaving intrusions produced by internal waves: a laboratory experiment. *J. Fluid. Mech.* **602**, 219–239.
- HUGHES, G. O. & GRIFFITHS, R. W. 2006 A simple convective model of the global overturning circulation, including effects of entrainment into sinking regions. *Ocean Modelling* **12**, 46–79.
- HUGHES, G. O. & GRIFFITHS, R. W. 2008 Horizontal convection. *Annu. Rev. Fluid Mech.* **40**, 185–208.
- HUGHES, G. O., GRIFFITHS, R. W., MULLARNEY, J. C. & PETERSON, W. H. 2007 A theoretical model for horizontal convection at high Rayleigh number. *J. Fluid. Mech.* **581**, 251–276.
- MULLARNEY, J. C., GRIFFITHS, R. W. & HUGHES, G. O. 2004 Convection driven by differential heating at a horizontal boundary. *J. Fluid. Mech.* **516**, 181–209.
- PAPARELLA, F. & YOUNG, W. R. 2002 Horizontal convection is non-turbulent. *J. Fluid. Mech.* **466**, 205–214.
- ROSSBY, H. T. 1965 On thermal convection driven by non-uniform heating from below: an experimental study. *Deep Sea Res.* **12**, 9–16.
- ROSSBY, H. T. 1998 Numerical experiments with a fluid non-uniformly heated from below. *Tellus* **50**, 242–257.
- SCHMITZ, W. J. 1995 On the interbasin-scale thermohaline circulation. *Rev. Geophys.* **33**, 151–173.
- WANG, W. & HUANG, R. X. 2005 An experimental study on thermal convection driven by horizontal differential heating. *J. Fluid. Mech.* **540**, 49–73.
- WONG, A. B. D. & GRIFFITHS, R. 1999 Stratification and convection produced by multiple plumes. *Dyn. Atmos. Oceans* **30**, 101–123.
- WONG, A. B. D., GRIFFITHS, R. W. & HUGHES, G. O. 2001 Shear layers driven by turbulent plumes. *J. Fluid. Mech.* **434**, 209–241.